Invited Paper

High performance GaInNAsSb/GaAs lasers at 1.5 μm

Lynford L. Goddard*, Seth R. Bank, Mark A. Wistey, Homan B. Yuen, James S. Harris Jr.
Solid State and Photonics Laboratory, 420 Via Ortega, Stanford University, Stanford, CA 94305

ABSTRACT

We achieved 1.5-μm CW SQW GaInNAsSb lasers with GaNAs barriers grown by MBE on GaAs substrates with typical room temperature threshold densities below 600A/cm^2, external quantum efficiencies above 50%, and output powers exceeding 200mW from both facets for 20x1222μm devices tested epitaxial-side up. In pulsed mode, 450A/cm^2, 50%, and 1100mW were realized. Longer devices yielded over 425mW of total CW power and thresholds below 450A/cm^2. These results are comparable to high quality GaInNAs/GaAs lasers at 1.3μm. Z-parameter measurements revealed that these improvements in the performance metrics of approximately 40-60% over previous results are primarily due to reduced monomolecular recombination. The large differential gain of GaInNAsSb/GaNAs/GaAs lasers at 1.5μm of approximately 1.2x10^{-15}cm^2 was mostly squandered in previous devices due to large quantities of monomolecular recombination. The characteristic temperatures for threshold current, T_0, and for efficiency, T_1, were 66K and 132K, respectively. These reduced values, compared to prior measurements of 106K and 208K, respectively, indicate carrier leakage. Since monomolecular recombination is temperature insensitive, the temperature stability of device operation was adversely affected.

Keywords: Semiconductor lasers, Raman amplifiers, Continuous-wave, GaInNAsSb, GaInNAs, GaAs, MBE, 1.5μm

1. INTRODUCTION

Low threshold, high power, continuous wave (CW) lasers near 1.5μm are required for pumping doped-fiber and Raman amplifiers. GaInNAs(Sb) edge-emitting lasers [1-10], vertical-cavity surface-emitting lasers (VCSEL) [11-15], and distributed feedback (DFB) lasers [16-17], grown monolithically on GaAs, have been demonstrated throughout the 1.2-1.6μm telecommunication bandwidth. They have several advantages over InP based devices: a larger conduction band offset which reduces temperature sensitivity and enhances differential gain, higher index contrast which decreases the necessary number of mirror pairs in distributed Bragg reflectors (DBRs) for VCSELs, native oxide apertures for current confinement, and lower cost wafers. The main issue has been the rapid degradation of material quality and device performance as the nitrogen concentration is increased to extend the lasing wavelength beyond 1.3μm. See Fig. 1.

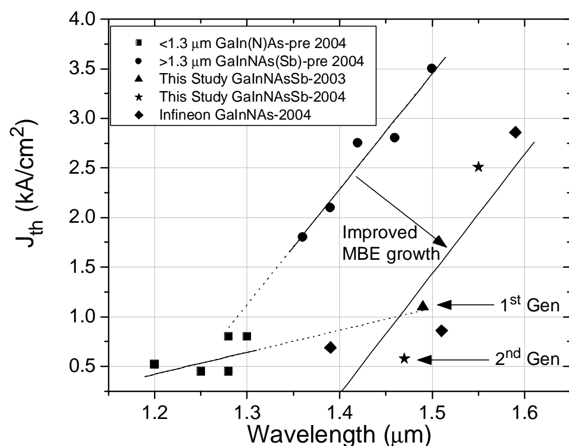

Figure 1: Threshold current density versus wavelength.

TABLE I: CAVITY LENGTH STUDY PARAMETERS

Parameter	Description
J_{th}	Threshold Current Density
η_e	External Quantum Efficiency
g_0	Gain Coefficient
J_{tr}	Transparency Current Density
J_{th}^{∞}	Infinite Cavity Length Threshold
η_i	Internal Quantum Efficiency
α_i	Internal Loss

* lgoddard@snow.stanford.edu; phone 1 650 725-6970 ext. 2; fax 1 650 723-4659

Novel In-Plane Semiconductor Lasers IV, edited by Carmen Mermelstein,
David P. Bour, Proceedings of SPIE Vol. 5738 (SPIE, Bellingham, WA, 2005)
0277-786X/05/$15 · doi: 10.1117/12.591447

High quality growth of GaInNAs(Sb) beyond 1.3µm has been challenging due to the large number of defects created by growing these highly metastable alloys at low temperatures. However, we have significantly reduced monomolecular recombination [18], the previous cause of high thresholds, by reducing ion-related damage during active layer growth [19-21] and minimizing defects by optimizing the rapid thermal annealing (RTA) process [21]. The reduced non-radiative recombination has also increased the differential quantum efficiency and output power.

This paper consists of eight sections. Throughout the paper, we will present results about devices labeled 2nd generation in Fig. 1 and compare the results to the previously reported results for 1st generation devices [8, 22, 23]. The main difference in the generations is the post-growth processing. Growth, fabrication, and testing details are discussed in Sec. 2. In Sec. 3, the room temperature (RT) device performance, i.e. *L-I-V* curves and spectra, is presented. We apply the method of Tansu and coworkers [24], which measures laser performance as a function of temperature and cavity length in Sec. 4. The method determines the characteristic temperature of intrinsic laser parameters described in Table I, such as g_0, J_{tr}, η_i, and α_i and was previously applied to 1st generation devices [23]. In Sec. 5, we discuss *Z*-parameter measurements, which track the dominant sources of recombination. In Sec. 6, we analyze the relative intensity noise (RIN) spectra and present additional intrinsic laser parameters, such as the differential and nonlinear gain coefficients. Initial reliability measurements are presented in Sec. 7. Sec. 8 summarizes the results.

2. GROWTH, FABRICATION, AND TESTING

Broad-area edge-emitting separate confinement heterostructure ridge-waveguide lasers were grown by solid-source MBE on (100) n-type GaAs. The growth and fabrication are described more fully in [8, 21]. Nitrogen was supplied with an rf plasma cell; deflection plates at the exit aperture, biased at –40V and ground, were used to minimize the ion flux upon the wafer [25, 9]. The 75Å $Ga_{0.62}In_{0.38}N_{0.023}As_{0.95}Sb_{0.027}$ single quantum well (SQW) was surrounded on both sides by 220Å $GaN_{0.025}As_{0.975}$ barriers that were embedded in a GaAs/$Al_{0.33}Ga_{0.67}As$ waveguide. The lasers were *ex-situ* annealed at 740°C for one minute in a rapid thermal annealing (RTA) furnace, with arsenic out diffusion minimized by a proximity cap. Ridges were defined with lift-off of Ti/Pt/Au Ohmic contacts, followed by a self-aligned dry etch to the top of the GaAs-waveguide. Samples were then thinned to ~120µm and Au/Ge/Ni/Au was evaporated onto the substrate side. A contact sinter was performed at 410°C for one minute. Devices of varying length were manually cleaved and soldered epi-side up on a temperature controlled copper heat sink. Unless otherwise specified, contact to the top p-metal was made at three locations along the device length with 24µm diameter Tungsten probe tips while contact to the n-metal was through the copper heat sink. At room temperature, lasing occurred at 1.46-1.48µm and 450-700A/cm^2, depending on device size and location on the wafer.

Testing was done under both CW and pulsed (1µs width, 1% duty cycle) conditions. The temperature dependent cavity length study was conducted in pulsed mode to avoid heating. However, the RIN and *Z*-parameter measurements were taken in CW mode to improve the measurement signal-to-noise and the accuracy of the applied current at the expense of about 5-10°C of device heating at threshold. We will denote the stage and active region temperatures by T_s and T_a, respectively. The thermal resistance, R_T, of our devices has been extensively measured [8]. For 20µm wide devices, the resistance in K/W is well modeled by R_T=30.3/L, where L is the device length in millimeters.

3. ROOM TEMPERATURE CHARACTERIZATION

Fig. 2 shows a typical CW *L-I-V* curve at RT (T_s=20°C) for a 20x1222µm device. At threshold, the current density was 580A/cm^2 and the voltage was 1.4V. The external quantum efficiency was 53% and the maximum power was 200mW from both facets. Peak CW output power was limited due to heating caused by the 1.6Ω series resistance and high thermal resistance, 24K/W, from mounting epi-side up. The series resistance, R_s, was about 0.4Ω lower than in comparable 1st generation devices, while the thermal resistance was about the same.

Fig. 3 is the optical spectra at three operation points marked in Fig. 2. The device lased at 1.465µm at threshold and at 1.50µm at maximum output power due to the 0.34meV/K bandgap reduction (0.58nm/K redshift) with temperature. The peak in the optical spectra at 6x threshold is only 40% greater than at 1.05x threshold despite the total output power being more than forty times larger. The peak intensity quickly saturates because of the large nonlinear gain compression coefficient ε, discussed in Sec. 6.

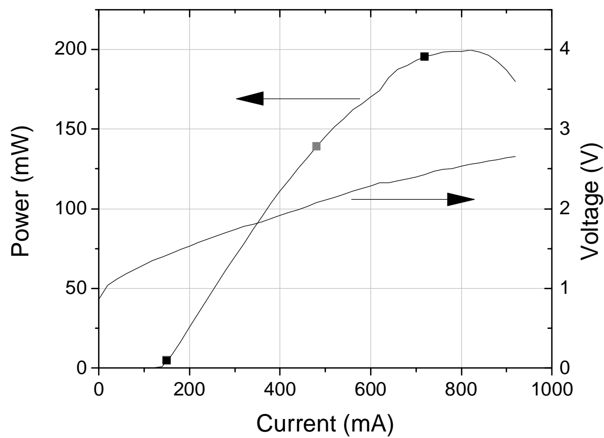

Figure 2: CW *L-I-V* curve for a 20x1222μm laser at 20°C.

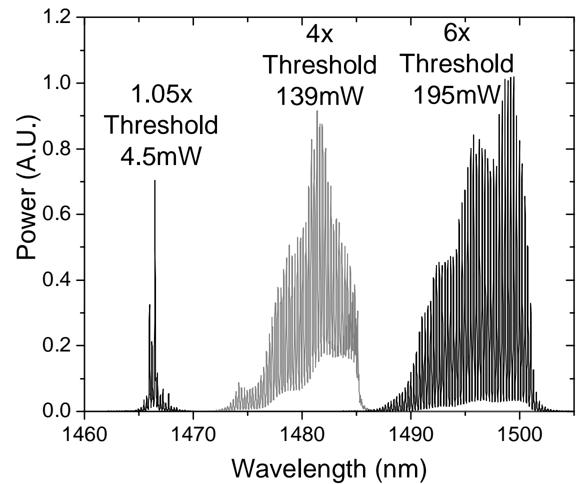

Figure 3: Optical spectra at various operation points.

Fig. 4 is the pulsed (400ns width, 0.1% duty cycle) *L-I-V* curve at RT for the same device. The threshold density was 450A/cm^2, the external quantum efficiency was 52%, and the maximum power was 1142mW from both facets. Peak pulsed output power was limited due to the 3A limit of the current driver.

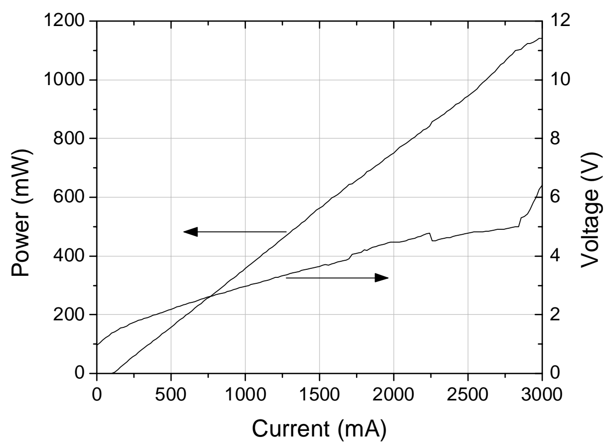

Figure 4: Pulsed *L-I-V* curve for a 20x1222μm laser at 20°C.

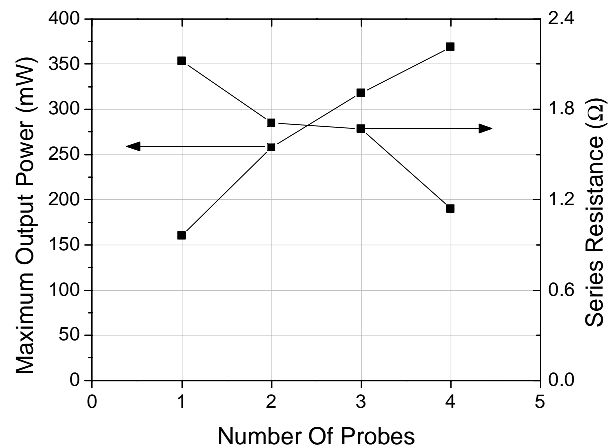

Figure 5: Dependence of P_{max} and R_s on number of probes.

To increase the maximum CW output power, P_{max}, improving the thermal and series resistance were investigated. There exists an optimal device length since the thermal conductance increases while the external efficiency decreases with length. Modeling the length dependence of the device parameters determined in Sec. 4 indicated that this optimal length is around 1900-2600μm for epi-up mounting. Devices with a size of 20x2150μm were processed. The contact resistance between the Tungsten probe tips and the Ti/Pt/Au p-metal as well as the longitudinal current spreading resistance of the ridge significantly affect the total series resistance. As illustrated in Fig. 5, increasing the number of probe contact points along the device length from 1 to 4 cut the device series resistance in half and more than doubled the output power.

Fig. 6 shows a CW *L-I-V* curve (T_s=15°C) for the 20x2150μm laser as the number of probe contact points is increased. The threshold density improved from 510 to 480A/cm^2 and the external quantum efficiency from 45 to 49% with increasing number of probes due to the slight reduction in device heating near threshold and more uniform current

injection. However, the most striking effect was the increase in power from 160 to 369mW as a result of the reduced series resistance. Fig. 7 is the optical spectra at three operation points along the 4 probe contact *L-I-V* curve. The lasing wavelength and its thermal broadening and redshift are similar to Fig. 3.

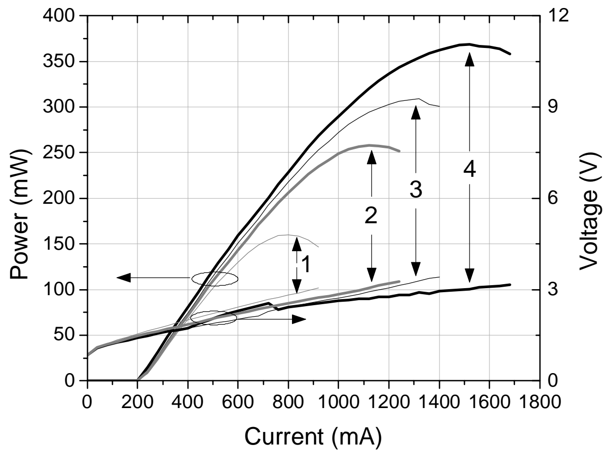

Figure 6: CW *L-I-V* curves for varying number of contacts.

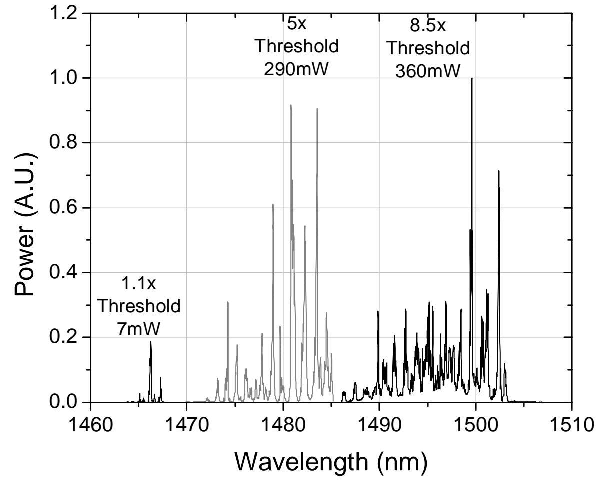

Figure 7: Optical spectra at various operation points.

Fig. 8 shows a CW *L-I-V* curve (T_s=15°C) of a nearby 20x2150μm laser with 5 probe contacts. The device was slightly better than the previous one, but was damaged a little (see kink in *I-V* curve) before a probe contact study could be performed. The device had a 440A/cm^2 threshold density at 1.32V and an external efficiency of 51%. A maximum of 431mW of power was obtained because R_s was reduced to 1.0Ω with the addition of the fifth probe. Output powers exceeding 500mW seem achievable if the number of contacts can be increased indefinitely, e.g. by using bond wire.

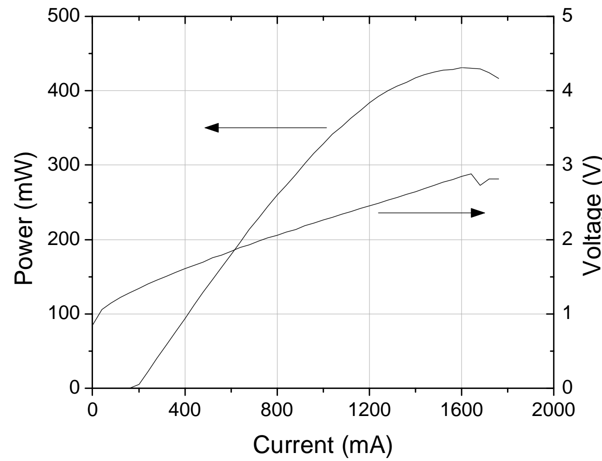

Figure 8: CW *L-I-V* curves with 5 probes at 15°C.

4. TEMPERATURE DEPENDENT CAVITY LENGTH STUDY

The derivation of the following laser equations is discussed more fully in [24, 23].

$$g = g_0 \ln\left(\frac{\eta_i J}{J_{tr}}\right) \quad (1)$$

$$J_{th} = \frac{J_{tr}}{\eta_i} \cdot \exp\left(\frac{\alpha_i + \alpha_m}{\Gamma \cdot g_0}\right) \quad (2)$$

$$\eta_e = \eta_i \cdot \frac{\alpha_m}{\alpha_i + \alpha_m} \quad (3)$$

where Γ=1.4% is the optical confinement factor, α_m=1/L ln(1/R) is the mirror loss, L is the cavity length, R=30% is the mirror reflectivity, g is the laser gain, J is the applied current density and the other parameters were defined in Table I. The temperature dependence of each parameter, x, in Table I is modeled by a local Arrhenius relation:

$$x(T) = x_0 \exp\left(\frac{\pm(T - T_{ref})}{T_x}\right) \quad (4)$$

where T is the temperature, T_{ref} is a reference temperature, and T_x and x_0 are the parameter's characteristic temperature and value at the reference temperature, respectively.

Low duty cycle pulsed *L-I-V* curves at T_s=15-75°C in 5°C steps were collected for 20µm wide devices with three cavity lengths: 1050, 1222, and 2150µm. Fig. 9 shows a set of *L-I* curves for a 2150µm device. For each temperature and cavity length, J_{th} and η_e were calculated from the *L-I* curve in the range of 4-12mW. To reduce the effect of variance in these measured parameters on the derived values for g_0, J_{tr}, J_{th}^{∞}, η_i, and α_i, the measured parameters were first fitted to local Arrhenius relations. The fitted values were then used in the cavity length calculations, i.e. fitting Equations (2) and (3), at each temperature. Fig. 10 shows such a fit for the device depicted in Fig. 9. Both parameters are well modeled by their Arrhenius fit over the entire 60K temperature range.

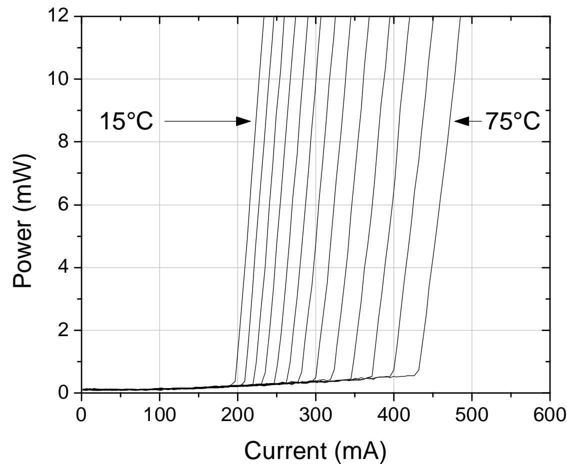

Figure 9: Temperature variation of *L-I* curves.

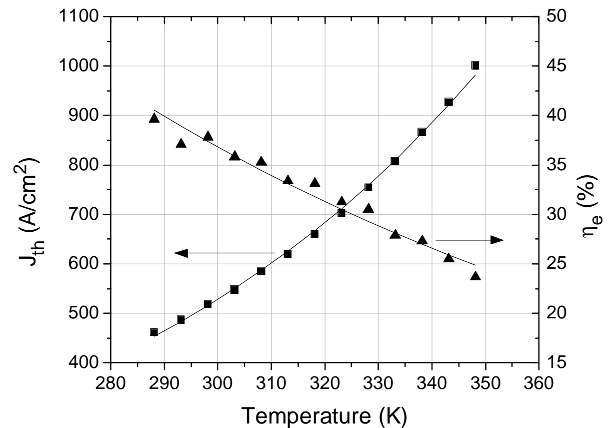

Figure 10: Temperature dependence of J_{th} and η_e.

Figs. 11 and 12 show the calculated values for g_0, J_{tr}, J_{th}^{∞}, η_i, and α_i versus temperature and their corresponding Arrhenius fits. The Arrhenius parameters are tabulated in Table II. The rapid decrease in g_0 is partly due to thermal broadening of the gain spectrum and increased occupation of higher quantized levels [26] and contributes to the rapid rise in J_{th}^{∞}. Carrier leakage and/or Auger recombination can also affect g_0. The increase in α_i is indicative of intervalence band absorption (IVBA) while the decrease in η_i is likely due to leakage/Auger recombination.

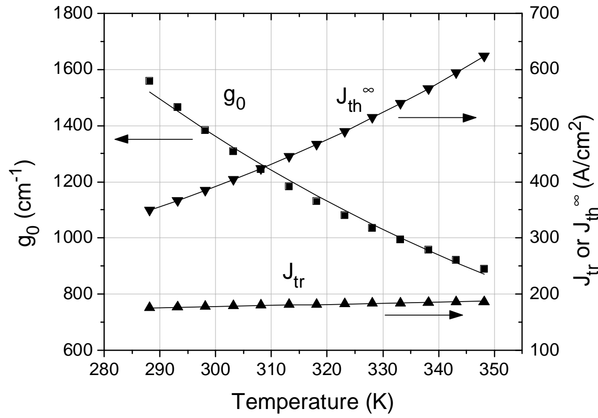

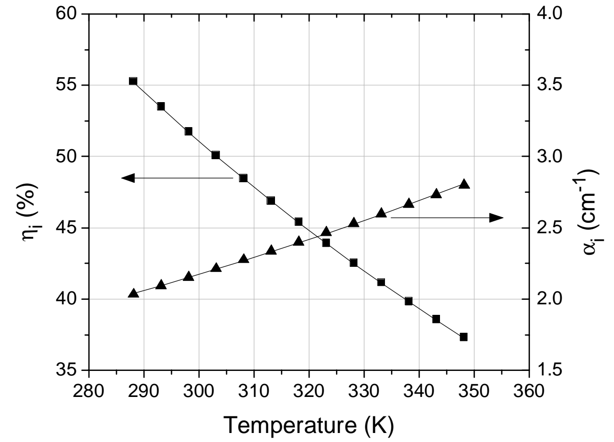

Figure 11: Temperature dependence of g_0, J_{tr}, and J_{th}^{∞}.

Figure 12: Temperature dependence of η_i and α_i.

TABLE II: MATERIAL AND DEVICE PARAMETERS RESULTS

Parameter	Value at RT	Characteristic Temperature
g_0	1440 ± 40 cm^{-1}	110 ± 6 K
J_{tr}	177 ± 8 A/cm^2	1000 ± 800 K
J_{th}^{∞}	366 ± 9 A/cm^2	104 ± 5 K
η_i	54 ± 3 %	153 ± 15 K
α_i	2.1 ± 0.4 cm^{-1}	188 ± 80 K

Measurement over a narrow 60K temperature range is insufficient to precisely determine the characteristic temperatures of weakly varying parameters, e.g. J_{tr}; the error bars increase rapidly with the value. Nevertheless, using the data in Table II, the cavity length dependence of the characteristic temperatures for J_{th} and η_e (T_0 and T_1, respectively) can be accurately predicted according to [24]:

$$\frac{1}{T_0} = \frac{1}{T_{tr}} + \frac{\alpha_i}{\Gamma \cdot g_0}\frac{1}{T_{\alpha_i}} + \frac{\alpha_i + \alpha_m}{\Gamma \cdot g_0}\frac{1}{T_{g_0}} + \frac{1}{T_{\eta_i}} \tag{5}$$

$$\frac{1}{T_1} = \frac{\alpha_i}{\alpha_i + \alpha_m}\frac{1}{T_{\alpha_i}} + \frac{1}{T_{\eta_i}} \tag{6}$$

The terms on the right hand side of Equations (5) and (6) have been arranged in order of increasing influence on the temperature sensitivity of J_{th} and η_e. The temperature sensitivity of η_i is responsible for low values of T_0 and T_1. In Fig. 8, the maximum CW output power occurred around 8.5x threshold. At this high bias, maintaining high efficiency as the device heats is critically important. If carrier leakage/Auger recombination can be reduced such that T_1 increases from 123K to 160K, P_{max} should increase by another 16% to over 500mW. The poor temperature performance of the gain coefficient g_0 also limits T_0. Values of T_0 around 85-90K are expected simply by applying an HR coating to the back facet of the 20x2150µm device.

The parameters T_0 and T_1 are expected to decrease slightly with temperature because of the temperature dependence of g_0 and α_i. The best prediction accuracy is obtained if the values for g_0 and α_i at the temperature midpoint of 45°C are used. Fig. 13 shows T_0 and T_1 and their predicted values as a function of cavity length.

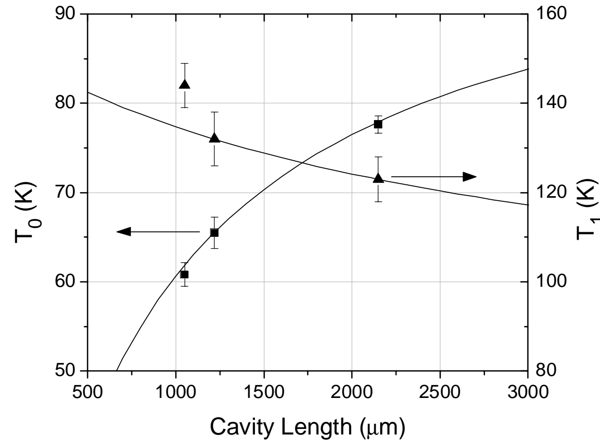

Figure 13: Cavity length dependence of T_0 and T_1.

5. Z-PARAMETER

The applied current *I* versus carrier density *n* relationship can be modeled locally by

$$I = \sum_{AllProcesses} c_{Process} n^{Z_{Process}} \tag{7}$$

where $c_{Process}$ and $Z_{Process}$ are constants [27]. In the non-degenerate limit, $Z_{Process}$=1, 2, or 3 for monomolecular, radiative, and Auger recombination, respectively. The local *Z*-parameter is defined as the instantaneous logarithmic derivative of *I* with respect to the integrated spontaneous emission rate *TSE* and equals the average effective *Z*-parameter of the constituent recombination processes [22],

$$Z \equiv \frac{d(\ln(I)}{d(\ln(TSE^{1/2}))} = \sum_{AllProcesses} Z_{Process}^{Effective} \frac{I_{Process}}{I_{Tot}} \tag{8}$$

In the degenerate limit, $Z_{Process}$ depends on *n* and its effective value at a given *n* is denoted by $Z_{Process}^{Effective}$.

Fig. 14 is a simulation of the behavior of $Z_{Process}^{Effective}$ (using its logarithmic derivative definition) versus carrier density for various mechanisms that might be significant in our devices: monomolecular recombination from midlevel traps in the QW, carrier leakage from electron traps in the GaNAs barriers caused by $(N\text{-}N)_{As}$ or $(As\text{-}N)_{As}$ interstitial defects, radiative recombination, and Auger CHCC or CHHS recombination. $Z_{Process}^{Effective}$ increases for carrier leakage processes because of degeneracy and the superlinear increase in the barrier population. It increases for Auger recombination because of the rapid increase in the population of carriers that can conserve energy and momentum. Since $Z_{Process}^{Effective} \geq 2$ for every process except monomolecular recombination from midlevel QW traps and $(N\text{-}N)_{As}$ traps near the conduction band edge, a measurement of $Z<1.5$ indicates that at least 50% of the current must be due to these traps.

The *Z*-parameter was measured for 1st generation devices [22] and 2nd generation devices [18]. The vertically emitted, unamplified, true spontaneous emission (*TSE*) exited the laser device through a 5µm square hole etched in the p-metal. It was then focused onto a fiber and integrated electrically with a relatively flat response InGaAs PIN detector. The experimental setup is described in more detail elsewhere [22].

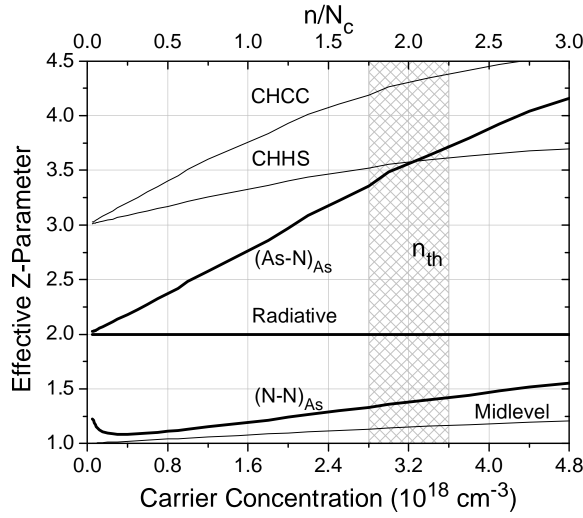

Figure 14: Simulation of $Z^{Effective}$ for various processes.

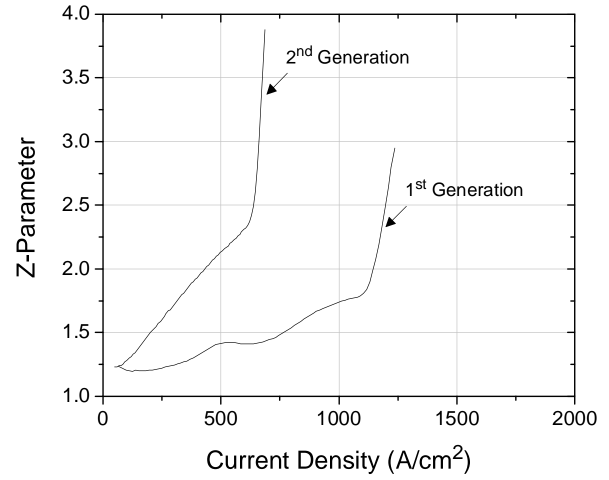

Figure 15: Comparison of measured *Z-J* curves at RT.

Fig. 15 is a comparison of the measured *Z*-parameter versus current density curves at RT. At threshold, the TSE weakly clamps and the *Z*-parameter diverges to $+\infty$. The sharp kink in *Z* indicates threshold. Below 200A/cm^2, both devices are dominated by trap recombination, however *Z* for the 1st generation sample remained below 1.5 beyond 650A/cm^2. At RT, the threshold Z-parameter, Z_{th}, was 1.8 and 2.4 for the 1st and 2nd generation samples respectively and J_{th} was 1100 and 630A/cm^2. Both generations were found to have approximately the same threshold carrier density n_{th} (shaded region in Fig. 14) and are therefore expected to have the same radiative and Auger current. At threshold, a possible distribution of current among trap, radiative, and Auger recombination that is consistent with these observations and Fig. 14 is 70 / 20 / 10% for the 1st generation devices and 50 / 35 / 15% for the 2nd generation devices. Thus, the great improvement in J_{th} and slight improvement in η_i are attributed to this reduction of monomolecular recombination.

6. RELATIVE INTENSITY NOISE

The relative intensity noise (RIN) spectra at several currents of a 10x1222μm device were measured at RT. The measurement technique is discussed in [28] and the characterized parameters and listed in Table III. Fig. 16 shows a RIN spectrum on a linear scale and its theoretical fit. The fit [29] determines f_r and γ at each current. Fig. 17 displays the RIN spectra at various currents on a log scale.

TABLE III: RELATIVE INTENSITY NOISE STUDY PARAMETERS

Parameter	Description
f_r	Resonance Frequency
γ	Damping Coefficient
P	Output Power Per Facet
D	Slope of f_r versus $\sqrt{P}$
K	Slope of γ versus f_r^2
γ_0	Threshold Damping Coefficient
τ_e^{th}	Threshold Differential Lifetime
dg/dn	Differential Gain
n_{tr}	Transparency Carrier Density
n_{th}	Threshold Carrier Density
ε	Nonlinear Gain Compression

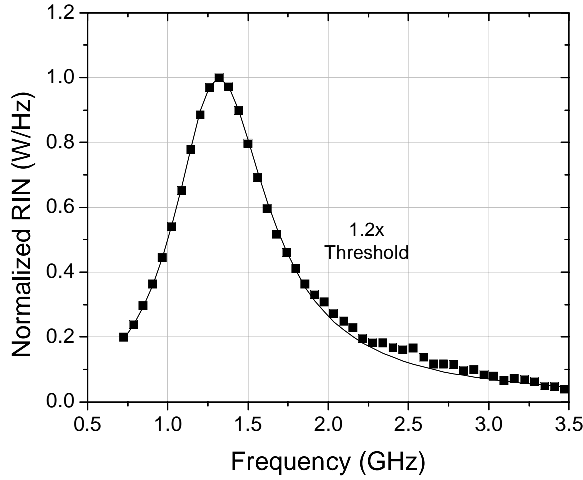

Figure 16: RIN spectrum (linear-scale) and its fit.

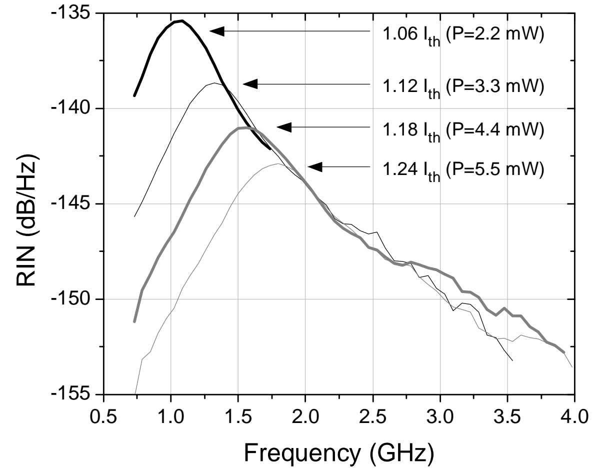

Figure 17: RIN spectrum (log-scale) for various currents.

Gain versus carrier density is modeled by a linear relationship with nonlinear gain compression that reduces the gain as the cavity photon density, N, is increased:

$$g(n) = \frac{dg}{dn}\frac{(n-n_{tr})}{1+\varepsilon N} \tag{9}$$

The RT values for dg/dn of 9.2x10^{-16}cm^2 and ε of 1.4x10^{-16}cm^3 were calculated through linear fits of f_r versus $\sqrt{P}$ and of γ versus f_r^2 [29, 30]:

$$f_r = D\sqrt{P} \tag{10}$$

$$\frac{dg}{dn} = \frac{1}{2}\frac{\alpha_m}{\alpha_m+\alpha_i}\frac{(h\nu)V_a(2\pi D)^2}{\Gamma v_g} \tag{11}$$

$$\gamma = Kf_r^2 + \gamma_0 \tag{12}$$

$$\varepsilon = \frac{dg}{dn}\left(\frac{Kv_g}{(2\pi)^2} - \frac{1}{\alpha_m+\alpha_i}\right) \tag{13}$$

where $h\nu$ is the photon energy, V_a is the active volume, and v_g is the group velocity. The f_r versus $\sqrt{P}$ and γ versus f_r^2 plots at RT are displayed in Figs. 18 and 19, respectively. The threshold differential carrier lifetime, τ_e^{th} = 1/γ_0, of 0.4±0.1 ns was also determined. The results for 1st generation devices were dg/dn=1.2x10^{-15} cm^2, ε=1.2x10^{-16}cm^3, and τ_e^{th}=3±2 ns. The intrinsic material parameters, dg/dn and ε are quite similar in the two generations of devices. Inaccuracy in determining γ_0, and therefore τ_e^{th}, was too large in the 1st generation of devices to be able to compare the threshold differential carrier lifetimes of the two device generations.

The GaInNAsSb/GaAs value for dg/dn at 1.5µm is comparable to the value of 1.06x10^{-15}cm^2 in GaInNAsSb/GaAs lasers at 1.26µm [31] and is significantly higher than the 5-7x10^{-16}cm^2 and 2-8x10^{-16}cm^2 for multiple quantum well (MQW) InGaAsP/InP lasers at 1.3µm [30] and 1.55µm [29]. At RT, n_{tr}=2.1x10^{18}cm^{-3} was measured and also calculated from the device band structure [22]. Equating gain to total loss at threshold, we calculate $n_{th}\approx$2.8-3.6x10^{18}cm^{-3} for both generations of devices, depending on the exact device length. The value for ε of 1.4x10^{-16}cm^3 is about 2x larger than for MQW $In_{0.35}Ga_{0.65}As$ lasers at 1080nm [32] and is probably due to strong inhomogeneous broadening, i.e. spectral hole burning within the energy bands. This greatly restricts additional stimulated emission at a given wavelength and explains the quick saturation of peak intensity observed in Figs. 3 and 7.

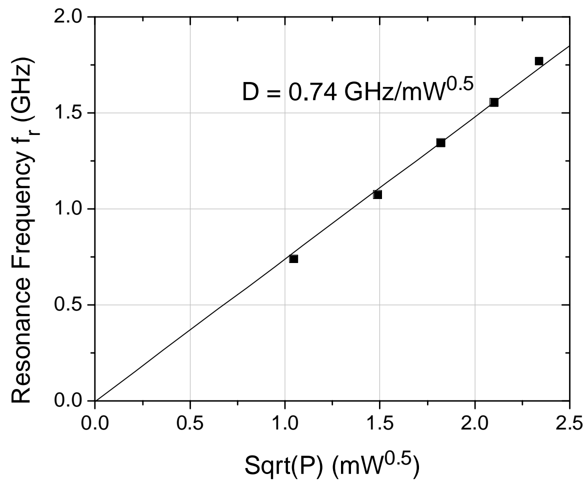

Figure 18: f_r versus $\sqrt{P}$ for a 10x1222μm device at RT.

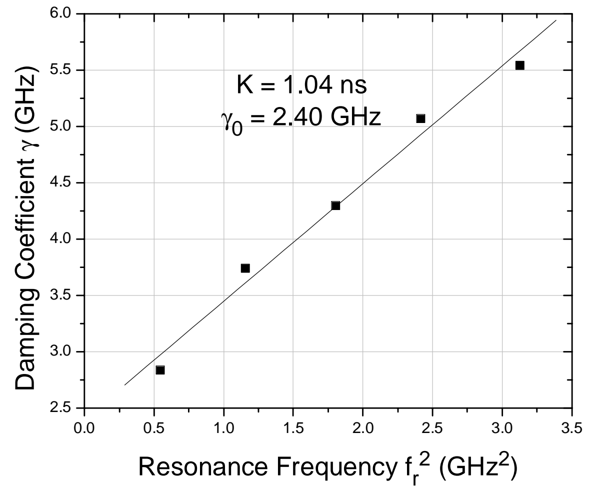

Figure 19: γ versus f_r^2 for a 10x1222μm device at RT.

7. RELIABILITY

A reliability study at high power operation is currently in progress. An unpackaged 20x2150μm device has operated at a constant CW output power of 200mW for over 90 hours with less than a 6% increase in operation current, I_{op}. See Fig. 20. The small jumps in operation correspond to changes in the ambient lab environment during the workday. The stage is cooled to T_s=0°C so that the active region temperature is close to RT during operation and the sample is probed at five locations.

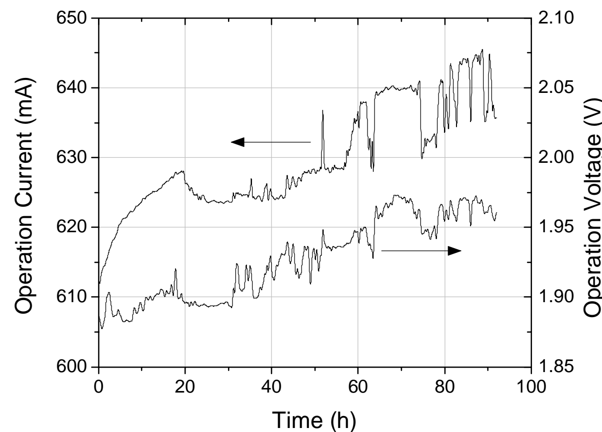

Figure 20: Time evolution of I_{op} and V_{op} for 200mW output.

The reliability of 2nd generation devices is greatly enhanced compared to 1st generation devices, where I_{op} increased by 70% after only 50 hours of operation at 10mW and T_s=15°C (T_a≈30°C). It was argued [22] that high levels of monomolecular recombination might enhance defect propagation by providing thermal energy during life testing. Also, through *Z*-parameter measurements, it was concluded that the primary source of device degradation of 1st generation devices was an increase in recombination through defects, especially the $(N\text{-}N)_{As}$ split interstitial. Thus, the vast improvement in reliability is also attributed to reduced monomolecular recombination.

8. CONCLUSION

Room temperature, CW, threshold densities below 500A/cm^2 and maximum output powers above 425mW at 1.5µm have been demonstrated from SQW GaInNAsSb lasers mounted epitaxial-side up. The improvements over our previous reports are primarily due to a reduction in the monomolecular recombination current and in the contact and series resistances. The large differential gain of GaInNAsSb at 1.5µm will be valuable for achieving high-speed operation. However, the temperature sensitivity of the internal efficiency was found to strongly influence the temperature stability of the threshold current and external efficiency. Further, the large nonlinear gain compression leads to saturation of peak laser emission intensity. Despite these drawbacks, GaInNAs(Sb) opto-electronic devices grown on GaAs may soon become widely commercialized throughout the 1.2-1.6µm telecommunication wavelength window due to their advantages over InP-based devices.

ACKNOWLEDGEMENT

The authors would like to thank Professor A. R. Adams at the University of Surrey, Professor N. Tansu at Lehigh University, and D. P. Bour of Agilent Technologies for discussions regarding Auger recombination, carrier leakage, IVBA, and the *Z*-parameter. The authors also wish to thank S. Zou of Santur Corp. for assistance in wafer thinning and facet coatings. The authors acknowledge A. Moto of Sumitomo Electric Industries for helpful discussions and donation of substrates. This work was supported under ARO, DARPA, and NSF grants DAAD17-02-C-0101, MDA972-00-1-024, and PHY-01-40297, as well as the Stanford Network Research Center (SNRC). L.L.G. acknowledges support from a National Physical Science Consortium Fellowship and stipend support from Xerox Palo Alto Research Center. S.R.B., M.A.W., and H.B.Y. each acknowledge Stanford University and NSF fellowship support over the years.

REFERENCES

1. M. Kondow, T. Kitatani, S. Nakatsuka, M. C. Larson, K. Nakahara, Y. Yazawa, M. Okai, and K. Uomi, "GaInNAs: a Novel Material for Long-wavelength Semiconductor Lasers," *IEEE J. Sel. Top. Quantum Electron.*, **3**, 719-730 (1997).
2. H. Shimizu, K. Kumada, S. Uchiyama, and A. Kasukawa, "High Performance CW 1.26 µm GaInNAsSb-SQW and 1.20 µm GaInAsSb-SQW Ridge Lasers," *Electron. Lett.*, **36**, 1701-1703 (2000).
3. N. Tansu and L. J. Mawst, "Low-threshold Strain-compensated InGaAs(N) (λ = 1.19-1.31 µm) Quantum-well Lasers," *IEEE Photon. Techol. Lett.*, **14**, 444-446 (2002).
4. W. Ha, V. Gambin, S. Bank, M. Wistey, H. Yuen, S. Kim, and J. S. Harris Jr., "Long-wavelength GaInNAs(Sb) Lasers on GaAs," *IEEE J. Quantum Electron.*, **38**, 1260-1267 (2002).
5. L. Li, V. Sallet, G. Patriarche, L. Largeau, S. Bouchoule, K. Merghem, L. Travers, J. C. Harmand, "1.5 µm Laser on GaAs with GaInNAsSb Quinary Quantum Well," *Electron. Lett.*, **39**, 519-520 (2003).
6. D. Gollub, S. Moses, M. Fischer, and A. Forchel, "1.42 µm Continuous-wave Operation of GaInNAs Laser Diodes," *Electron. Lett.*, **39**, 777-778 (2003).
7. S. Bank, M. Wistey, H. Yuen, L. Goddard, W. Ha, and J. S. Harris Jr., "Low-threshold CW GaInNAsSb/GaAs Laser at 1.49µm," *Electron. Lett.*, **39**, 1445-1446 (2003).
8. S. Bank, M. Wistey, L. Goddard, H. Yuen, V. Lordi, and J. S. Harris Jr., "Low-threshold Continuous-wave 1.5-µm GaInNAsSb Lasers Grown on GaAs," *IEEE J. Quantum Elect.*, **40**, 656-664 (2004).
9. S. Bank, M. Wistey, L. Goddard, H. Yuen, H. Bae, and J. S. Harris Jr., "High-performance 1.5 µm GaInNAsSb Lasers Grown on GaAs," *Electron. Lett.*, **40**, 1186-1187 (2004).
10. R. Averbeck, G. Jaschke, L. Geelhaar, and H. Riechert, "Low Threshold InGaAsN/GaAs Lasers Beyond 1500 nm," *ICMBE Conf.*, Edinburgh, Scotland (2004).
11. C. Coldren, M. Larson, S. Spruytte, and J. S. Harris, "1200 nm GaAs-based Vertical Cavity Lasers Employing GaInNAs Multiquantum Well Active Regions," *Electron. Lett.*, **36**, 951-952 (2000).
12. K. Choquette, J. Klem, A. Fischer, O. Blum, A. Allerman, I. Friz, S. Kurz, W. Breiland, R. Sieg, K. Geib, J. Scott, and R. Naone, "Room Temperature Continuous Wave InGaAsN Quantum Well Vertical-cavity Lasers Emitting at 1.3 µm," *Electron. Lett.*, **36**, 1388-1390 (2000).

13. G. Steinle, H. Riechert, and A. Yu. Egorov, "Monolithic VCSEL with InGaAsN Active Region emitting at 1.28 μm and CW Output Power Exceeding 500 μW at Room Temperature," *Electron. Lett.*, **37**, 93-95 (2001).
14. T. Takeuchi, Y. Chang, M. Leary, A. Tandon, H. Luan, D. Bour, S. Corzine, R. Twist, and M. Tan, "1.3 μm InGaAsN Vertical Cavity Surface Emitting Lasers Grown by MOCVD," *Electron. Lett.*, **38**, 1438-1440 (2002).
15. M. Wistey, S. Bank, H. Yuen, L. Goddard, and J. S. Harris, "Monolithic, GaInNAsSb VCSELs at 1.46μm on GaAs by MBE," *Electron. Lett.*, **39**, 1822-1823 (2003).
16. M. Reinhard, M. Fischer, M. Kamp, J. Hofmann, and A. Forchel, "1.3-μm GaInNAs–AlGaAs Distributed Feedback Lasers," *IEEE Photon. Tech. Lett.*, **12**, 239-241 (2000).
17. D. Gollub, M. Kamp, A. Forchel, J. Seufert, S. Bank, M. Wistey, L. Goddard, H.Yuen, and J.S. Harris, "Continuous-Wave Operation of GaInNAsSb Distributed Feedback Lasers at 1.5 μm," *Electron. Lett.*, **37**, 1487-1488 (2004).
18. L. Goddard, S. Bank, M. Wistey, H. Yuen, H. Bae, and J. S. Harris Jr., "Reduced Monomolecular Recombination in GaInNAsSb/GaAs Lasers at 1.5μm," *LEOS Conf.*, Rio Grande, PR, session MO 6 (2004).
19. M. Wistey, S. Bank, H. Yuen, and J. S. Harris, "Reduced Damage During Growth of GaInNAs Using Low Voltage Ion Deflection Plates," *submitted to Appl. Phys. Lett*.
20. M. Wistey, S. Bank, H. Yuen, L. Goddard, and J. S. Harris, "Protecting Wafer During Plasma Ignition by Use of an Arsenic Cap," *submitted to J. Vac. Sci. Tech.-B*.
21. S. Bank, M. Wistey, H. Yuen, L. Goddard, H. Bae, and J. S. Harris, "MBE Growth of Low-Threshold CW GaInNAsSb Lasers at 1.5 μm," s*ubmitted to J. Vac. Sci. Tech.-B.*
22. L. Goddard, S. Bank, M. Wistey, H. Yuen, Z. Rao, and J. S. Harris Jr., "Recombination, Gain, Band Structure, Efficiency, and Reliability of 1.5μm GaInNAsSb/GaAs Lasers," *submitted to J. Appl. Phys*.
23. S. Bank, L. Goddard, M. Wistey, H. Yuen, and J. S. Harris Jr., "On the Temperature Sensitivity of 1.5μm GaInNAsSb Lasers," *submitted to IEEE J. Sel. Top. Quantum Electron.*
24. N. Tansu, Y. Chang, T. Takeuchi, D. Bour, S. Corzine, M. Tan, and L. Mawst, "Temperature Analysis and Characteristics of Highly Strained InGaAs-GaAsP-GaAs (lambda > 1.17 μm) Quantum-well Lasers," *IEEE J. Quantum Electron.*, **38**, 640-651 (2002).
25. M. A. Wistey, S. R. Bank, H. B. Yuen, and J. S. Harris, "Real-Time Ion Count from Nitrogen Plasma Source," *North American MBE Conf.*, session P2-9 (2003).
26. L. Goddard, S. Bank, M. Wistey, H. Yuen, and J. S. Harris Jr., "Analysis of the Temperature Dependence of Gain in 1.5μm GaInNAsSb Lasers," *to be submitted to Appl. Phys. Lett*.
27. A. F. Phillips, S. J. Sweeney, A. R. Adams, and P. J. A. Thijs, "The Temperature Dependence of 1.3- and 1.5-μm Compressively Strained InGaAs(P) MQW Semiconductor Lasers," *IEEE J. Sel. Topics Quantum Electron.*, **5**, 401-412 (2002).
28. L. Goddard, S. Bank, M. Wistey, H. Yuen, H. Bae, and J. S. Harris Jr., "Differential Gain and Non-linear Gain Compression of GaInNAsSb/GaAs Lasers at 1.5μm," *submitted for presentation at CLEO Conf.* (2005).
29. M. Tatham, I. Lealman, C. Seltzer, L. Westbrook, D. Cooper, "Resonance Frequency, Damping, and Differential Gain in 1.5μm Multiple Quantum-Well Lasers," *IEEE J. Quantum Elect.*, **28**, 408-414 (1992).
30. N. Yokouchi, N. Yamanaka, N. Iwai, Y. Nakahira, and Akihiko Kasukawa, "Tensile-Strained GaInAsP-InP Quantum-Well Lasers Emitting at 1.3μm," *IEEE J. Quantum Elect.*, **32**, 2148-2155 (1996).
31. H. Shimizu, K. Kumada, S. Uchiyama, and A. Kasukawa, "Extremely Large Differential Gain of 1.26μm GaInNAsSb-SQW Ridge Lasers," *Electron. Lett.*, **37**, 28-30 (2001).
32. J. Ralston, S. Weisser, I. Esquivias, E. Larkins, J. Rosenzweig, P. Tasker, and J. Fleissner, "Control of Differential Gain, Nonlinear Gain, and Damping Factor for High-Speed Application of GaAs-Based MQW Lasers," *IEEE J. Quantum Elect.*, **29**, 1648-1659 (1993).